

Wiley International Journal of Energy Research Volume 2025, Article ID 4252866, 17 pages https://doi.org/10.1155/er/4252866



Research Article

Binary Transition Metal and Nitrogen Functionalised Silicon Oxycarbide Electrocatalysts for Zn-Air Battery Air Electrode Application

Marek Mooste , ^{1,2} Rohit Kumar, ² Silver Juvanen, ² Jekaterina Kozlova, ³ Arvo Kikas, ³ Alexey Treshchalov, ³ Maike Käärik, ² Jaan Aruväli, ⁴ Jaan Leis, ² Vambola Kisand, ³ Kaupo Kukli, ³ Dana Schonvogel, ¹ Peter Wagner, ¹ Michaela Wilhelm, ⁵ Kaido Tammeveski , ² and K. Andreas Friedrich ⁶

Correspondence should be addressed to Marek Mooste; marek.mooste@ut.ee and Kaido Tammeveski; kaido.tammeveski@ut.ee

Received 3 April 2025; Revised 21 August 2025; Accepted 22 September 2025

Academic Editor: Zhien Zhang

Copyright © 2025 Marek Mooste et al. International Journal of Energy Research published by John Wiley & Sons Ltd. This is an open access article under the terms of the Creative Commons Attribution License, which permits use, distribution and reproduction in any medium, provided the original work is properly cited.

The need for the wider adoption of next-generation energy storage systems due to the usage of renewable energy encourages the development of alternatives to the lithium-ion battery (LIB) technology. Rechargeable zinc–air battery (RZAB) could meet this objective as affordable, safe, and material abundant alternative if suitable non-Pt group metal (PGM) air electrode bifunctional catalyst for oxygen reduction reaction (ORR) and oxygen evolution reaction (OER) is developed. Herein, we investigate three binary transition metal (TM) combinations (Fe/Co, Fe/Mn, Fe/Cu) for the polymer-derived ceramics (PDCs)-based bifunctional catalyst fabrication. Dicyandiamide (DCDA) was used as a nitrogen source for the dual TM-containing PDC material modification. The highest electrocatalytic activity towards the ORR/OER in 0.1 and 1.0 M KOH was witnessed in the case of Fe/Co-containing material (Fe/Co-PDC-N, ORR/OER potential gap in 0.1 M KOH of 0.87 V), which was also the most promising non-PGM catalyst in the RZAB configuration. Fe/Co-PDC-N showed the maximum power density of 142 mW cm⁻², 46 h lifetime for 10 mA cm⁻² charge–discharge cycling and 97% depth of discharge (DoD). Comparative RZAB measurements were performed with the commercial Pt-Ru/C catalyst drawing attention to the performance enhancement implemented by the RZAB cell design modifications.

Keywords: electrocatalysis; non-precious metal catalyst; oxygen evolution reaction; oxygen reduction reaction; Zn-air battery

1. Introduction

Rechargeable zinc—air battery (RZAB) could be a viable alternative for lithium-ion battery (LIB) in electric vehicles (EVs), portable electronics and renewable energy devices due to their potential to provide a clean and sustainable next generation energy storage system [1]. The need for the latter is especially important for EVs if the production ban on fossil-fuel vehicles

in 2035 is implemented [2, 3]. The advantages of RZAB over LIB are cost-effectiveness, safety and higher theoretical energy density (1353 Wh kg_{Zn}^{-1} [1]), whereas the latter making them more energy-efficient [1, 4]. The working principle of RZAB relies on the bifunctional electrocatalytic activity for oxygen reduction reaction (ORR) and oxygen evolution reaction (OER) of the air electrode and for which an alternative is needed to phase out expensive and rare Pt-group metal

¹Institute of Engineering Thermodynamics, German Aerospace Center (DLR), Oldenburg, Germany

²Institute of Chemistry, University of Tartu, Tartu, Estonia

³Institute of Physics, University of Tartu, Tartu, Estonia

⁴Institute of Ecology and Earth Sciences, University of Tartu, Tartu, Estonia

⁵Advanced Ceramics, University of Bremen, Bremen, Germany

⁶Institute of Engineering Thermodynamics, German Aerospace Center (DLR), Stuttgart, Germany

(PGM)-based electrocatalysts (e.g., Pt/C, Pt-Ru/C, IrO₂, RuO₂) [5, 6].

The RZAB air electrode catalyst material should catalyse the ORR via direct $4e^-$ or $2\times 2e^-$ reaction pathway with the final product of HO $^-$. Moreover, the $2e^-$ ORR route should be avoided due to the lower energy efficiency and final product of highly reactive HO_2^- , which could harm the RZAB components. The OER reaction pathway in RZAB is opposite to the $4e^-$ pathway of the ORR, converting HO^- ions to H_2O and O_2 while releasing the electrons [1, 4].

A viable alternative to PGM catalysts are the non-precious metal catalysts (NPMCs), which are based on the nanocarbon support materials with high specific surface area (e.g., carbon nanotubes [CNTs], graphene-based carbons, conducting polymers, etc.) [7, 8, 9, 10]. To achieve a high bifunctional activity towards oxygen reactions, the heteroatom doping (e.g., N, S) with accompanying transition metal (TM, e.g., Fe, Co) is a crucial addition [4, 5]. Most importantly, this approach provides highly active and desired N-coordinated TM centres $(M-N_x)$ [11, 12, 13], while also the doping of nanocarbons with nitrogen species (e.g., pyridinic-N, pyrrolic-N, graphitic-N) itself is beneficial for ORR/OER in alkaline environment. Specifically, the described N-based active sites help to modulate the electronic properties of carbon to promote the adsorption of O₂ molecule and the breaking of O=O bond [14]. In recent years, the focus has been turned to the double TM (e.g., Fe/Co) and N co-doped nanocarbons [15, 16, 17], which could surpass the ORR/OER activity of a single TM-containing (e.g., Fe-N-C) catalysts [18, 19, 20, 21] and with atomically dispersed dual atom sites can have a potential for industrial scale catalyst production [22].

In several investigations, the affordable and easily available nitrogen source dicyandiamide (DCDA) has been used for the N-functionalisation of TM-containing nanocarbons, and the obtained catalysts have shown promising results for ORR/OER in alkaline environment [23, 24]. DCDA-derived various single TM (e.g., Fe, Cu, Mn, Co) and binary Fe/Co containing NPMCs have been already investigated at the RZAB air electrode [20, 24], but there is currently no information available for the air electrode performance comparing various double TM combinations within a single investigation (Fe/Co, Fe/Cu, Fe/Mn) to determine the superior TM combination for this specific catalyst application. Furthermore, polymer-derived ceramics (PDCs) subclass silicon oxycarbide (SiOC), which have good chemical and thermal stability, superior oxidation and corrosion resistance in harsh conditions, have already been shown to be a suitable NPMC backbone for renewable energy applications, for example, RZAB [25, 26] and fuel cells [23, 27]. Therefore, SiOC is an excellent candidate for N-doped binary TM air electrode catalyst fabrication.

In addition to the bifunctional activity of NPMC at the air electrode towards the ORR/OER, other RZAB components (e.g., Zn anode, electrolyte) can have a significant effect on the cell performance. For example, conventional alkaline electrolytes in RZAB suffer from zincate precipitation and carbonation, affecting their charge—discharge lifespan [4]. Furthermore, the parasitic reactions with the Zn electrode

include anodic hydrogen evolution reaction (HER) and subsequent H₂ release into the cell [28, 29], Zn passivation [30, 31] and corrosion [32]. All these problems should be considered and possibly mitigated as much as possible to enable the air electrode ORR/OER performance-dependent RZAB system.

In the present investigation, the binary TM and N codoped PDC-based NPMCs for liquid RZAB were prepared using DCDA and Fe/Co, Fe/Cu, Fe/Mn combinations for the first time within one work. The preliminary electrocatalyst ORR/OER activity evaluation was performed in the 0.1 and 1.0 M KOH solution, while the RZAB testing with commercial Pt-Ru/C catalyst for comparison was performed in a RZAB cell configuration with a modified design (electrolyte chamber ventilation, more efficient Zn electrode utilisation). The Pt-Ru/C data for the original cell version was also published together with the possible explanations for the observed benefits introduced by the RZAB cell modifications.

2. Materials and Methods

2.1. Material Preparation. The procedure for preparing binary TM-containing PDC-based catalyst precursor materials was obtained from a recent report [33]. Poly(methyl phenyl silsesquioxane) (H44, Wacker Chemie AG), silicon resin poly(methylsilsesquioxane) (MK, Wacker Chemie AG), graphite (IMERYL Graphite & Carbon), azodicarboxamide (Azo, Sigma-Aldrich), (3-Aminopropyl)triethoxysilane (APTES), xylene (Sigma-Aldrich), imidazole (Imi, Alfa Aesar), copper(-II) 2,4-pentanedionate (CuAc, 98%, abcr GmbH), iron(II) acetylacetonate (FeAc, 95%, abcr GmbH), manganese(II) acetylacetonate (MnAc, Sigma Aldrich), cobalt(II) acetylacetonate (CoAc, Sigma Aldrich) were used for the precursor catalyst material preparation as shown in Table S1 in the Supporting Information. The chemicals were mixed and subjected to pyrolysis under a N2 atmosphere, then crushed manually and finally ball-milled (PM 400, Retsch) at 350 rpm to produce a fine powder according to already reported route [33]. The sieved fraction (particle sizes <100 µm) was used for the catalyst preparation and these materials are denoted by the pair of TMs followed by "PDC" (Table S1).

The N functionalisation of the four different PDC materials (Table S1) was adapted from a recent work [33]. DCDA (99%, Sigma–Aldrich) was employed as a N source as in the report by Canuto de Almeida e Silva et al. [23] with few alterations (e.g., solvent, pyrolysis temperature). In brief, 1:20 weight ratio of PDC:DCDA mixture was dispersed in methanol (99.9%, Thermo Scientific Chemicals) via sonication for 2 h followed by evaporation of the methanol at 60°C. The dry mixture was pyrolysed in N_2 environment using the tube furnace with a ceramic tube (RHTC 80–230/15, Nabertherm) and heating rate of 5°C min $^{-1}$ until 900°C, followed by the dwelling time of 2 h at the latter temperature. For the optimisation, carbonisation at 800°C was also used. The obtained materials have -N in their designation, for example, Fe/Co-PDC-based catalyst is named Fe/Co-PDC-N after N functionalisation [23].

2.2. Physical Characterisation. Micro-Raman spectra were recorded in the back-scattering geometry on an inVia Renishaw spectrometer in conjugation with a confocal

3

microscope (Leica Microsystems CMS GmbH), 50× objective and an argon ion laser operated at 514.5 nm. To avoid thermal decomposition of the sample, the laser power density was minimised by decreasing the laser power and defocusing. All samples were suspended in 2-propanol and drop-coated on silicon substrates. The first-order Raman spectra of the catalysts was normalised to the intensity of the G band. The spectrum processing involved a baseline correction and multiple-peak fitting procedure using the PeakAnalyser software in OriginPro 9. In the curve-fitting procedure, all parameters (peak position, height and width) were adjusted to attain the smallest value of the chi-square. The Raman spectra were fitted following the five-peak Voigt-shaped band model where G peak (~1590 cm⁻¹) corresponds to the stretching vibrations of the sp² carbon atoms in the ideal graphitic lattice; D1 (~1350 cm⁻¹) to defect-activated breathing mode of aromatic rings; D2 (~1620 cm⁻¹) disordered graphitic lattice (surface graphene layers, E_{2 g}-symmetry); D3 (1490 cm⁻¹) to amorphous carbon and D4 (1210 cm⁻¹) to disordered graphitic lattice [34]. The defects in the as-synthesised catalysts were evaluated using the $I_{\rm D1}/(I_{\rm G}+I_{\rm D2})$ ratio (integrated areas under the bands).

The surface morphology of the samples was analysed using scanning electron microscopy (SEM) with a Helios Nanolab 600 (FEI) microscope operated at 10 kV. The elemental composition was determined using an INCA Energy Dispersive X-ray Spectrometer (EDX, Oxford Instruments) coupled to the same microscope, which was operated at an accelerating voltage of 15 kV.

Scanning transmission electron microscopy (STEM) was conducted using a Titan Themis 200 (FEI) microscope at 200 kV. Simultaneously, bright-field (BF) and high-angle annular dark-field (HAADF) images were collected from the same locations on the sample. Elemental distribution in the samples was studied using EDX in STEM mode, employing a Super-X EDX system (FEI/Bruker) coupled to the STEM and recorded using Esprit software. For STEM analysis, the sample suspension in isopropanol was drop-cast onto holey carbon-coated copper TEM grids (or gold grid for copper-containing sample).

X-ray photoelectron spectroscopy (XPS) studies were performed with an SCIENTA SES-100 spectrometer using 200 eV pass energy with glassy carbon plates coated with the catalyst ink prepared in 2-propanol. The electron take-off angle was 90°. The non-monochromatic Mg K_{α} X-ray source (1253.6 eV) was used in the case of Fe/Mn-PDC-N and Fe/Co-PDC-N samples, while Al K_{α} X-ray source was used for the Fe/Cu-PDC-N. The pressure inside the analysis chamber was below 10^{-9} mbar during data collection. The raw data were processed using Casa XPS software (version 2.3.17) and involved removal of X-ray satellites, peak fitting using the Gauss–Lorentz hybrid line shapes and combination of linear and Shirley backgrounds.

The N_2 adsorption—desorption measurements and X-ray diffraction (XRD) analyses were performed using the experimental setup and conditions reported in an earlier study [18].

2.3. Electrochemical Characterisation

2.3.1. Half-Cell Studies in KOH Solutions. The rotating disc electrode (RDE) and cyclic voltammetry (CV) experiments were performed in a 3-electrode configuration using Autolab

potentiostat PGSTAT302N (Metrohm Autolab, The Netherlands), Nova 2.1 software, EDI101 rotator and CTV101 (Radiometer) speed control unit. The investigations were conducted in Ar-saturated (99.999 %, Linde) or O2-saturated (99.999 %, Linde) 0.1 and 1.0 M KOH (p.a. quality, Merck) with saturated calomel electrode (SCE) as the reference electrode and Pt-wire as a counter electrode. All the reported potentials are converted to the reversible hydrogen electrode (RHE) calculated using the equation: $E_{\text{RHE}} = E_{\text{SCE}} + 0.241 + 0.059 \times \text{pH}$. Polished and ultrasonically cleaned [35] glassy carbon (GC, $A = 0.196 \text{ cm}^2$) electrodes (GC-20SS, Tokai Carbon, Japan) served as the working electrode covered with the NPMC ink with a loading of $0.2 \,\mathrm{mg}\,\mathrm{cm}^{-2}$. The catalyst ink was prepared by 1 h sonication of 5 mg catalyst in 750 µL 2-propanol (99.8 %, Honeywell Riedelde Haën) and 12.5 µL 5% Nafion (Ion Power Inc.) solution. The Pt-Ru/C catalyst (40 wt% Pt, 20 wt% Ru on 50% compressed carbon clack, HiSPEC 10300, Thermo Scientific) was coated on the GC electrode with 20 μg_{Pt} cm⁻² loading. Polarisation curves for ORR and OER were recorded in the cathodic and anodic directions, respectively, and corrected for iR-drop similarly to the previous investigation [24]. The electrochemical double layer capacitance (C_{dl}) was calculated at different potential scan rates (ν) of 10–60 mV s⁻¹ in the non-faradaic region and potential window of 200 mV using the equation [36]:

$$C_{\rm dl} = \frac{\Delta j}{\nu},\tag{1}$$

where Δj is the average value of cathodic (j_c) and anodic (j_a) current density $(\Delta j = 0.5 \times (j_a - j_c))$ determined on the CV curve measured at 0.915 V vs. RHE.

2.3.2. RZAB Measurements. An in-house built liquid electrolyte RZAB setup from previous investigations [24, 37, 38] was modified for the present work with following additions. Firstly, the freshly polished Zn-foil (99.9%, Auto-plaza, 0.2 mm thick) electrode was pierced with a 4 mm diameter hole punch, which enables electrolyte contact on both sides of the Zn-foil increasing the total Zn electrode area to 6.04 cm² and total electrolyte volume to ca. 4 mL. The weight of the corresponding Zn-foil outlined with rubber O-rings available for electrolyte contact was 0.431 g. Secondly, the electrolyte compartments (connected by 4 mm diameter hole) at both sides of the Zn-foil were vented to the MilliQ water filled airlock with polytetrafluoroethylene (PTFE) tubes to prevent possible gas overpressure during the battery operation. The air electrode with 0.79 cm² active geometric area was prepared according to the previous investigations [24, 37, 38] using Sigracet BB39 gas diffusion layer (GDL) coated with the catalyst ink prepared as the mixture of catalyst powder, water, ethanol, and 5% Nafion solution. The final NPMC and Pt-Ru/C catalyst loading at the air electrode was 1.8 and 1.2 mg cm⁻², respectively. The final catalyst loading after drop-casting and drying in the oven was confirmed by microwave plasma atomic emission spectrometry (MP-AES) analysis. An aqueous solution of 6 M KOH + 0.2 M Zn(CH₃COO)₂·2H₂O (Fisher Scientific, 98%) was used as the electrolyte.

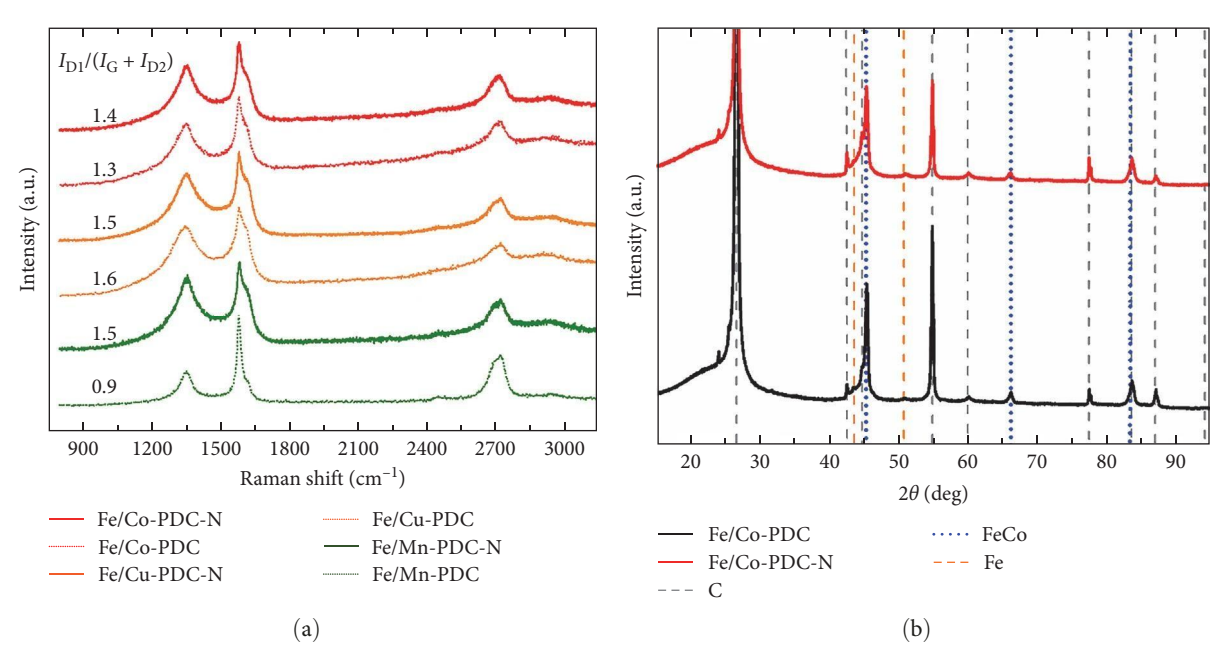


FIGURE 1: (a) Raman spectra and calculated $I_{\rm D1}/(I_{\rm G}+I_{\rm D2})$ ratios for unmodified double TM-containing PDC materials and their DCDA functionalised derivatives (-N), (b) XRD patterns for Fe/Co-PDC(-N) catalysts and XRD peak positions for C (graphite; PDF 04-013-0293), FeCo (Fe_{0.33}Co_{0.67}, PDF 04-021-8467), Fe (PDF 01-081-8775).

The discharge and charge polarisation curves for the RZAB were recorded in galvanostatic mode with a scan rate of -10 and $10 \, \text{mA min}^{-1}$, respectively. In addition, the primary battery voltage drop during the total discharge over time was measured using a current density of $-20 \, \text{mA cm}^{-2}$. The RZAB testing was performed by continuous charge–discharge cycling with $-10 \, \text{mA cm}^{-2}$ for $0.5 \, \text{h}$ and $+10 \, \text{mA cm}^{-2}$ for another $0.5 \, \text{h}$ resulting in 1 h total one cycle length. The cut-off voltage for RZAB tests was below $0.2 \, \text{V}$ and over $3.5 \, \text{V}$ for discharging and charging experiments, respectively. The RZAB cell was breathing to the open atmosphere during all types of measurements. The used and reported current density values for RZAB experiments have been calculated with respect to the active geometric area of the air electrode.

3. Results and Discussion

3.1. Physical Characterisation of the Catalysts. Raman spectroscopy analysis was performed to investigate the influence of nitrogen functionalisation with DCDA via pyrolysis on the carbon structure in the PDC samples (Figure 1a). This route is known to introduce new carbon material (e.g., CNTs) if TM nanoparticles (NPs) are present in the precursor mixture [39, 40, 41]. To investigate the degree of graphitisation, the I_{D1} / (I_G+I_{D2}) ratios were used for more accurate assessment (Figure S1). The precursor PDCs exhibited rather various $I_{D1}/(I_G+I_{D2})$ ratios of 0.9-1.6 depending on the pair of used TMs and after N functionalisation very similar ratios of 1.4-1.5 were observed. High $I_{D1}/(I_G+I_{D2})$ ratio and significant broadening of D1 band indicate the presence of defective graphitic carbon structures due to the functionalisation procedure [34]. This observation indicates the possibility for rather similar new carbon material (e.g., CNTs) formation among all the PDC materials during the

high-temperature decomposition of DCDA. The $\rm N_2$ adsorption–desorption measurements were conducted to evaluate the influence of N modification on PDC materials in more detail (Figure S2). In the case of double TM-containing PDC materials, the very similar Brunauer–Emmett–Teller (BET) surface area ($\rm S_{BET}$) values around 60 m 2 g $^{-1}$ were calculated before and after the DCDA functionalisation except for Fe/Cu-PDC ($\rm 72~m^2~g^{-1}$) and Fe/Cu-PDC-N ($\rm 128~m^2~g^{-1}$). The latter result is similar to the zeolitic imidazolate framework-8 (ZIF-8) modified binary TM-containing PDC materials from earlier report ($\rm 130-140~m^2~g^{-1}$) [33], while the values around 60 m 2 g $^{-1}$ for other catalysts are also higher than the ones previously reported for DCDA functionalised single TM-containing PDC materials [23].

For the determination of crystalline phases in the catalysts, the XRD analyses were performed with double TM-containing PDC materials before and after the functionalisation with DCDA (Figures 1b, S3). The N doping has no distinctly recognisable effect on the crystalline composition of the materials. As a common component, the graphitic carbon is observed with the most intense XRD peak at 26.5° in every diffractogram familiar from previous studies of similarly prepared PDC catalysts [23, 33]. Therefore, this peak exceeds the shown intensity scale maximum, so that all the other reflections can be well noticed in the XRD patterns. In the case of Fe/Co materials, only the peaks of FeCo alloy and Fe NPs are observed indicating the presence of both types of NPs. In the case of Fe/Cu and Fe/Mn materials, the peaks of crystalline TM oxides are also observed in addition to the both types of NPs, single TM and TM alloys.

The surface morphology and bulk composition of the precursor and N-modified PDC materials were further investigated using SEM and EDX methods. The structure and

., Wiley Online Library on [27/10/2025]. See the Terms and Conditions (https://onlinelibrary.wiley.com/terms-and-conditions) on Wiley Online Library for rules of use; OA articles are governed by the applicable Creative Commons

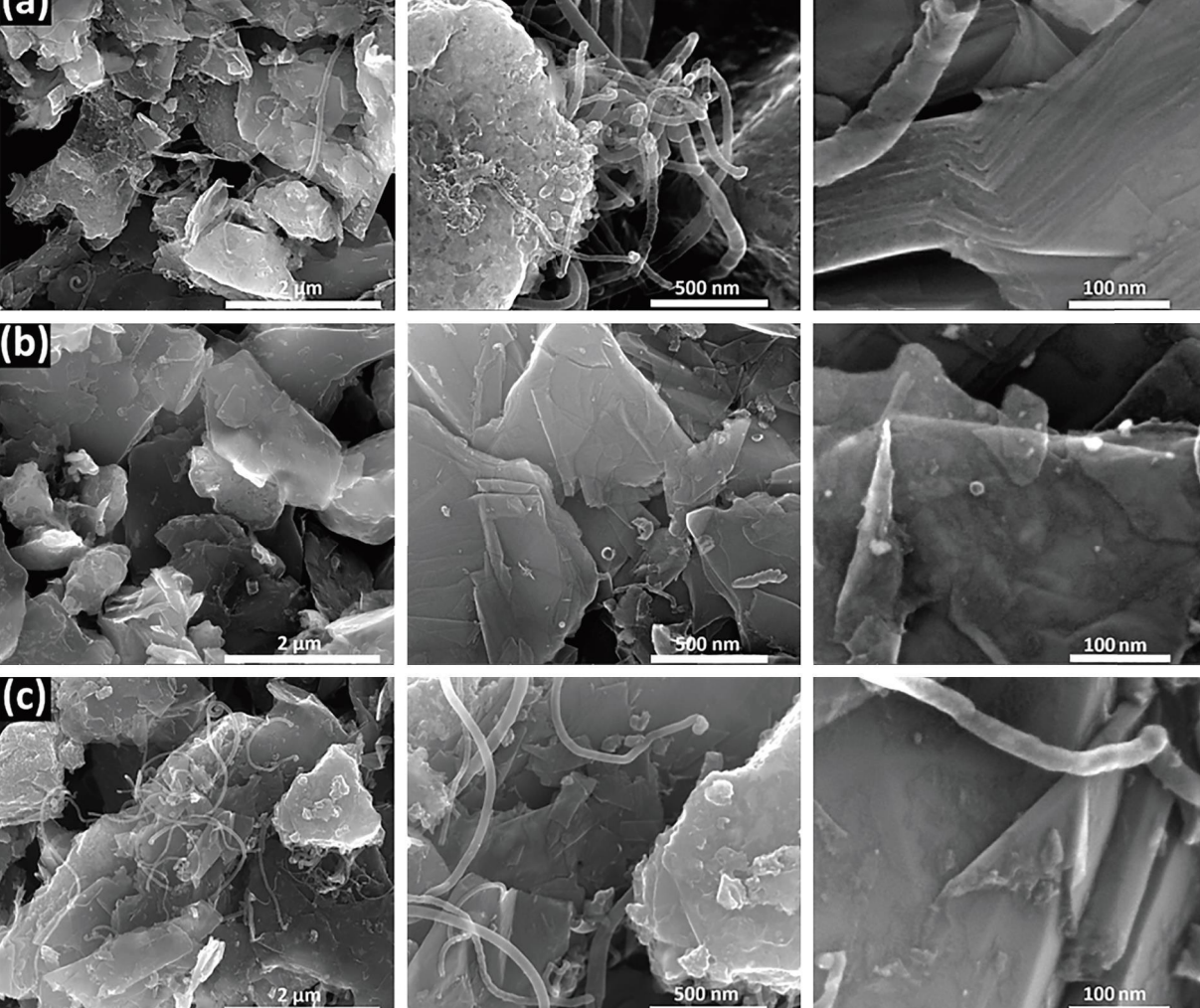


FIGURE 2: SEM micrographs with different magnifications of (a) Fe/Co-PDC-N, (b) Fe/Cu-PDC-N, (c) Fe/Mn-PDC-N catalysts.

composition of the precursor PDC materials (Figures S4, S5; Table S2) is in accordance with the data reported for single and double TM-containing PDC powders reported in early [23] and more recent [33] studies, respectively. Modification of binary TM-containing PDCs with DCDA has no observable influence at the ~ 100 µm scale (Figure S4), while the formation of CNTs is clearly observed for Fe/Co-PDC-N and Fe/Mn-PDC-N catalysts at the higher magnifications (Figure 2a–c). This is supported by the observed $I_{D1}/(I_G+I_{D2})$ ratio of 1.4–1.5 obtained by Raman spectroscopy (Figure 1a). Furthermore, a considerable increase in the N content is observed (Tables 1, S2) as expected similarly to the single TM-containing PDC material modification with DCDA in an earlier investigation [23], which in turn confirms the successful N-functionalization. Fe/Co-PDC-N exhibits the highest N content (4.63 wt%), while the amount of all TMs in the samples is rather uniform (~1.3-1.6 wt%) among 3 N-modified PDC catalysts (Table 1). During the precursor mixing and functionalisation procedures, the contaminants of Ca and K have been also

introduced into the PDC catalysts, while these elements are not known to affect the ORR and OER performance of the NPMC materials.

STEM images and STEM-EDX mappings were acquired to investigate the nature of the TMs embedded into the PDC materials functionalised with N using DCDA (Figures 3, S6, S7). STEM images showed the presence of TM NPs of various sizes (~10–200 nm) within the catalyst materials (Figure 3a,c) and at the ends of CNTs for Fe/Co-PDC-N (Figure 3a) as TM NPs are known to catalyse the CNT growth [42]. Furthermore, the TM NPs are covered with graphitic carbon layers (Figure 3a,c, highest magnification) very similarly to the ones in Fe, Co, and N co-doped graphene-coated alumina nanofibers prepared in our earlier investigation using DCDA as an N source [24]. The nature of the TM NPs was further evaluated using the STEM-EDX elemental mapping (Figure 3b), which indicated the presence of TM alloy NPs (Figure S6). The signal from the covering carbon layers are similarly registered for both, Fe/Co and Fe/Mn alloy NPs, while the ratio of metals

jer, 2025, I. Downloaded from https://onlineibtary.wiley.com/doi/10.1155/e/4252866 by Disch Zentrum F. Luft-U. Raum Fahrt In D. Helmholtz Gemein., Wiley Online Library or 127/10/2025, See the Terms and Conditions (https://onlineibtary.wiley.com/terms-and-conditions) on Wiley Online Library for rules of use; OA articles as governed by the applicable Centeive Commons License

Table 1: Bulk elemental composition of different double TM containing and N-doped PDC materials determined from the EDX analysis (wt %).

Catalyst material	С	N	0	Si	Ca	K	Fe	Со	Cu	Mn
Fe/Co-PDC-N	65.94	4.63	14.94	11.48	0.33	0.10	1.28	1.29	0	0
Fe/Cu-PDC-N	64.59	2.59	16.64	11.56	1.47	0.20	1.41	0	1.57	0
Fe/Mn-PDC-N	66.71	2.25	14.39	13.12	0.35	0.10	1.48	0	0	1.59

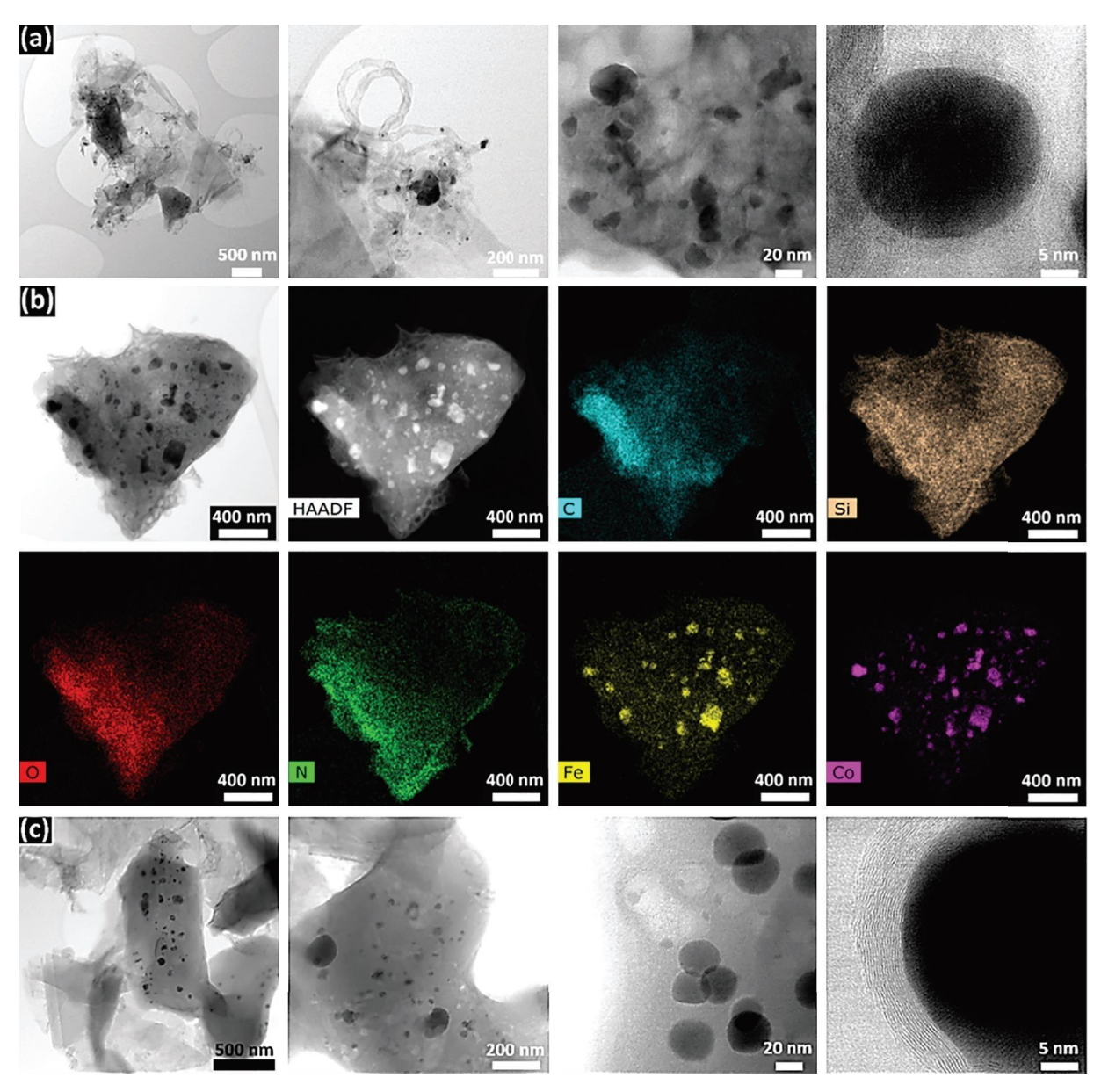


FIGURE 3: Bright-field (BF) STEM images with different magnification for (a) Fe/Co-PDC-N, (c) Fe/Cu-PDC-N. (b) BF and high-angle annular dark field (HAADF) STEM images with EDX elemental maps for Fe/Co-PDC-N catalyst.

in NPs aligns well with the XRD results (Figures 1b, S3). The Fe/Co NPs have 1/3 ratio of the corresponding TMs, while Fe/Mn have Fe as the major component.

The absence of strong O signal from these TM NP sites shows most likely the low amount or absence of TM oxides within the TM NPs (Figure 3b). The well-scattered O signal can

result from uniformly distributed metal oxides according to EDX analyses (Figure S3) and from O in the PDC backbone (SiOC). Additionally, the EDX mapping revealed the rather uniform presence of both TM and N signals in the catalyst material (Figures 3b, S7). This could indicate the existence of the dispersed TM sites and possibly dual TM sites, which are

ijer, 2025, 1, Downloaded from https://onlinelibrary.wiley.com/doi/10.1155/er/4.923866 by Disch Zentrum F. Luft-U. Raum Fahrt In D. Helmholtz Gemein, Wiley Online Library on [27/10/2025]. See the Terms and Conditions (https://onlinelbrary.wiley.com/crms-and-conditions) on Wiley Online Library for rules of use; OA articles are governed by the applicable Creative Commons License

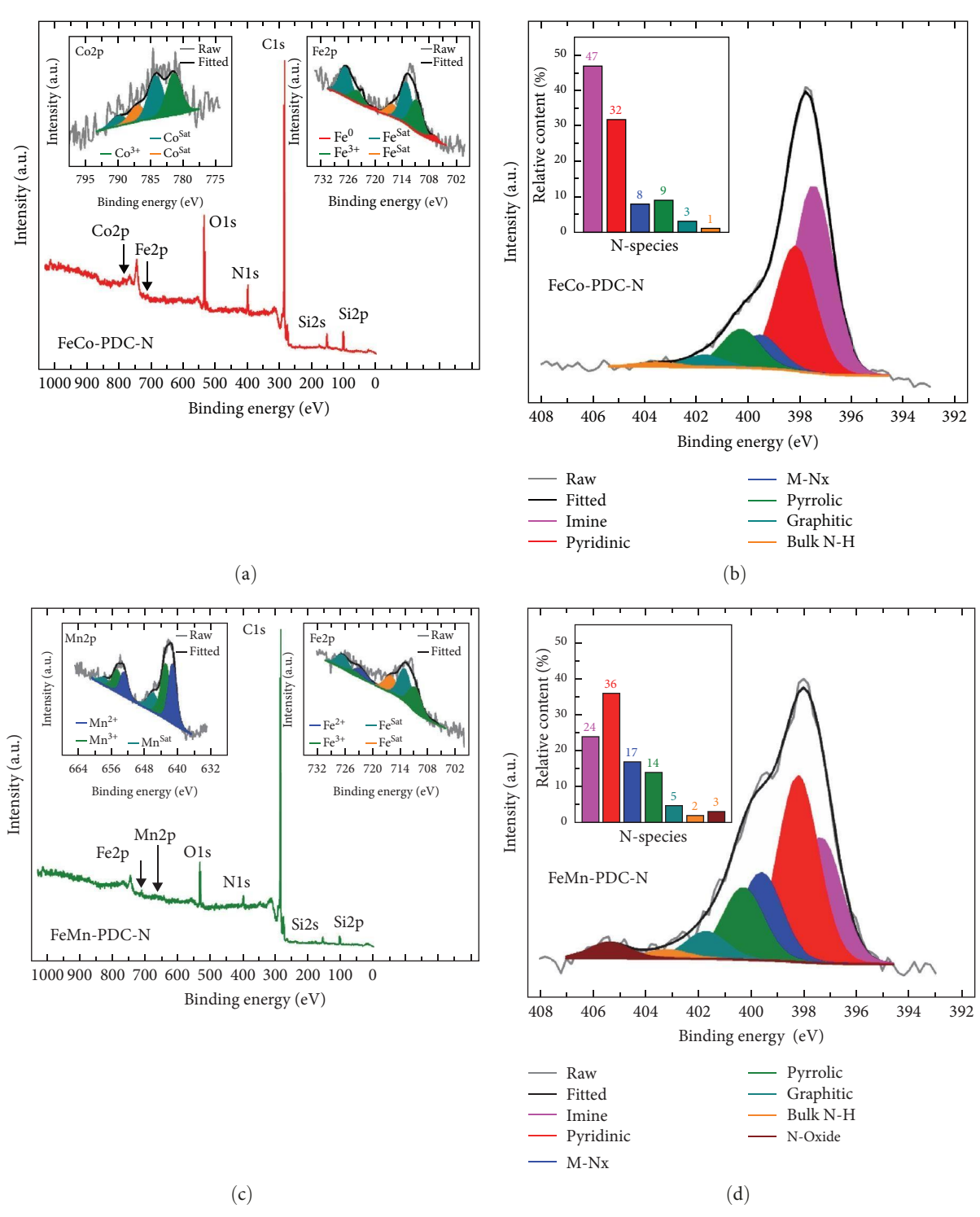


Figure 4: Continued.

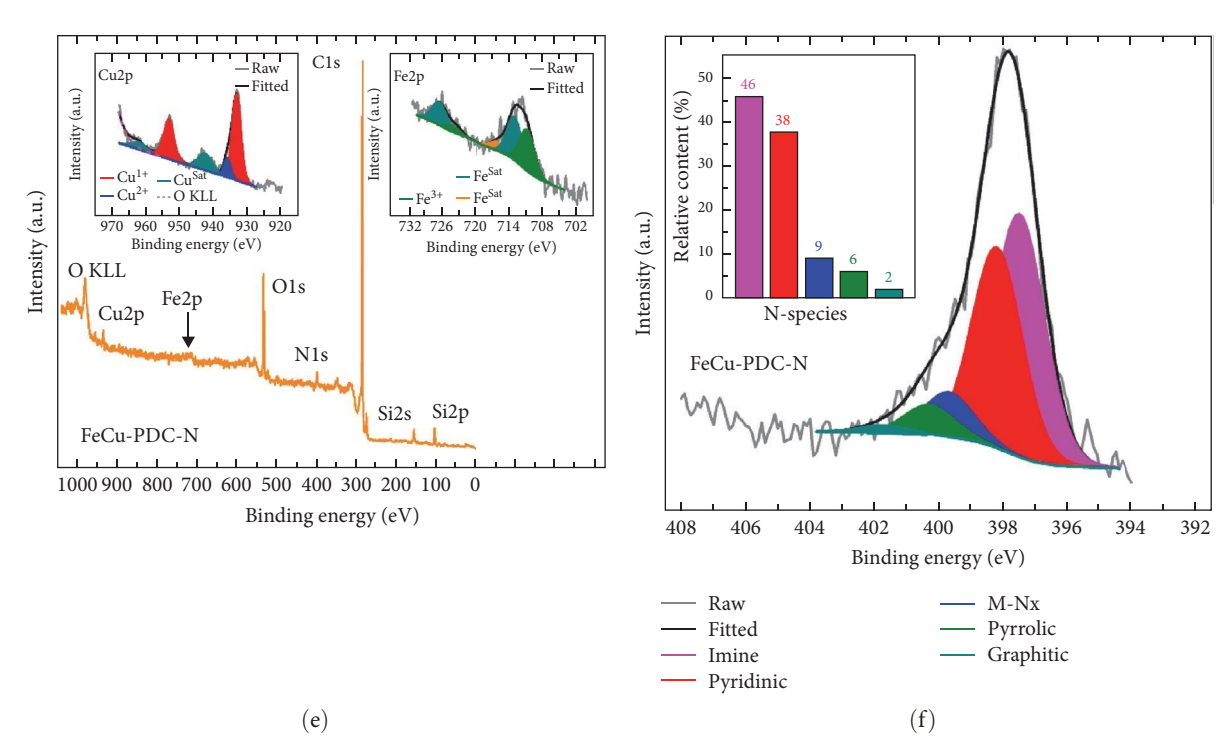


FIGURE 4: (a, c, e) XPS survey spectra and (insets) high-resolution XPS spectra in the Fe2p and (a) Co2p, (c) Mn2p, (e) Cu2p region with deconvoluted peaks, (b, d, f) high-resolution XPS spectra in the N1s region with deconvoluted peaks and (insets) relative content (%) of various N species for different double TM-containing and N-doped PDC materials.

Table 2: Surface elemental composition (at%) of different double TM containing and N-doped PDC materials determined from the XPS data shown in Figure 4.

Catalyst	Si	C	N	О	Ca	Fe	Cu	Co	Mn
Fe/Co-PDC-N	7.34	73.4	5.32	13.18	0.36	0.29	0	0.13	0
Fe/Cu-PDC-N	4.58	78.83	1.97	12.87	0.65	0.16	0.94	0	0
Fe/Mn-PDC-N	3.12	85.85	2.84	7.39	0.30	0.20	0	0	0.32

highly desirable from ORR electrocatalysis point of view [20, 43, 44].

The surface composition and atomic bonding configuration of the as-prepared catalyst materials were further investigated using the XPS technique (Figure 4, Table 2). XPS revealed the presence of the same elements (Figure 4a,c,e) as identified by EDX analysis (Table 1), similar to previous investigations of mono- and bimetallic PDC catalyst materials [23, 27, 33]. From the active sites responsible for ORR and OER electrocatalysis, the most important components are the N and the binary TMs.

The N1s spectra of the catalysts were deconvoluted to seven species similarly as in the previous investigations of TM and N functionalised NPMCs [18, 24, 45, 46]. Imine (~397.4 eV), pyridinic (~398.2 eV), M-N $_{\rm x}$ (~399.6 eV), pyrrolic (~400.3 eV), graphitic (~401.7 eV), bulk N—H (~403.4 eV), and N-oxide (~405.4 eV). The relative content (%) of each N functionality is given in the insets to Figure 4b,d,f. Among all 3 N-modified binary TM-containing PDC materials, the pyridinic N shows similar high relative content of 32%–38%, which is often considered as the most active N species for ORR and OER electrocatalysis

according to several investigations [14, 47]. Fe/Mn-PDC-N shows the highest relative amount of pyrrolic N and M-N_x, which are also considered favourable for the high electrocatalytic activity of both oxygen reactions, while M-Nx is especially important due to the possible origin from N coordinated to atomically dispersed single or dual TM sites [12, 20, 48, 49, 50]. Although, it should be considered that due to the close XPS peak overlapping, the pyridinic N and pyrrolic N can also include the contribution from the M-N_x sites and vice versa [51]. Furthermore, the graphitic N with relatively low content of 2%–5% among three materials could lower the ORR onset and half-wave potentials, while increasing HO₂⁻ yield in alkaline media [52]. It should be noted that the total amount of N is 2.7 and 1.9 times higher in Fe/Co-PDC-N catalyst compared to the Fe/Cu-PDC-N and Fe/Mn-PDC-N materials, respectively. This trend is in accordance with the EDX data (Table 1) and results in the total amount of all N components being significantly higher in the Fe/Co catalyst providing the possibility for a much larger total amount of N-based active sites for ORR and OER compared to the other binary TM materials.

om/terms-and-conditions) on Wiley Online Library for rules of use; OA articles are governed by the applicable Creative Commons

jer, 2025, 1, Downloaded from https://onlinelibrary.wiley.com/doi/10.1155/er/4252866 by Dtsch Zentrum F. Luft-U. Raum Fahrt In D. Helmholtz Gemein., Wiley Online Library on [27/10/2025]. See the Terms

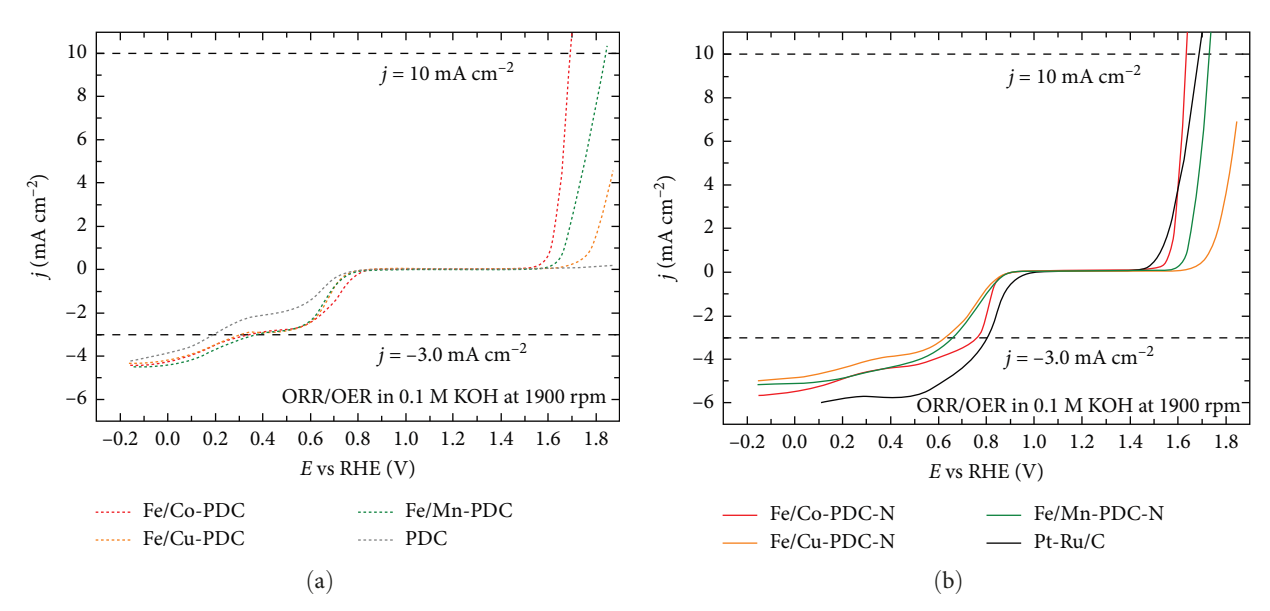


FIGURE 5: Combined RDE voltammetry curves for oxygen reduction and evolution reaction on different (a) precursor PDC material, (b) N-functionalised PDC catalyst and Pt-Ru/C-coated electrodes in O₂-saturated 0.1 M KOH solution ($\nu = 10 \text{ mV s}^{-1}$) at 1900 rpm, NPMC loading 0.2 mg cm⁻², Pt-Ru/C loading 20 μ gpt cm⁻².

The deconvolution of TM 2p spectra is complicated due to the low amount of TMs and high noise in the XPS spectra. However, it can be assumed from the insets to Figure 4a,c,e, that all TMs are rather in an oxidised state than in zero-valent metallic form. TMs in oxidised state are characteristic to the M-N $_{\rm x}$ centres, where they can be coordinated by N [53, 54]. It should be noted that in addition to M-N $_{\rm x}$ centres, the oxidised TM can be present in the TM oxides as confirmed by XRD analyses (Figure S3), which are considered beneficial for high OER activity according to the literature [8, 55].

3.2. RDE and CV Studies in KOH Solutions. The preliminary characterisation of the ORR (Figure S8) and OER performance was conducted via half-cell studies using the RDE technique in the O₂-saturated 0.1 M KOH electrolyte at 1900 rpm. The ORR route of the metal-free and double TM-containing precursor PDC materials followed the 2e⁻ reduction pathway from ca. 0.5 to 0.3 V vs. RHE and increased towards 4e (or 2 × 2e) at lower potentials from 0.3 to -0.2 V (Figure 5a, Table 3). This kind of electrocatalytic behaviour is inherent to the metal-free and single TM-containing PDC materials without additional N functionalisation as documented in several previous studies [23, 25, 26]. Modification with N using DCDA considerably increased the ORR activity of the catalysts (Figure 5b, Table 3) as expected according to the previous work with single TMcontaining PDCs [23]. The highest electrocatalytic activity towards the ORR among three binary TM combinations is observed in the case of Fe/Co-containing catalyst material (Fe/Co-PDC-N, $E_{1/2} = 0.76 \text{ V}$). Although, it should be noted that the $E_{1/2}$ value for Pt-Ru/C (0.80 V, similar to previous reports [24, 25]) is not reached. As a general observation over different reaction environments and N sources, the gas diffusion electrode half-cell studies in acidic conditions at 160°C in our recent investigation also revealed the Fe/Co combination showing the highest ORR activity over Fe/Mn and

Table 3: The ORR half-wave potential at -3 mA cm⁻² ($E_{1/2}$), the OER potential at the current density of 10 mA cm⁻² ($E_{j=10}$) and the ORR/OER potential gap ($\Delta E = E_{j=10} - E_{1/2}$) values for Pt-Ru/C and different PDC-based catalyst-coated GC electrodes obtained in this study (Figure 5) and from the literature [25, 27].

Catalyst	E _{1/2} (V)	$E_{j=10} (V)$	Δ E (V)
Pt-Ru/C	0.80	1.69	0.89
Fe/Co-PDC	0.33	1.69	1.36
Fe/Co-PDC-N	0.76	1.63	0.87
Fe/Mn-PDC	0.37	1.84	1.48
Fe/Mn-PDC-N	0.67	1.73	1.06
Fe/Cu-PDC	0.31	_	_
Fe/Cu-PDC-N	0.63	_	_
5 wt%-Ni/PDC [25]	0.62	1.61	0.99
Ni/SiOC [27]	0.73	1.62	0.89

Fe/Cu in the case of ZIF-8 modified binary TM-containing PDC material [33].

To investigate the ORR kinetics and pathway for Fe/Co-PDC-N catalyst in more detail, the RDE voltammetry curves at various rotation rates (ω) were recorded and the Koutecky-Levich (K-L) plots were constructed (Figure 6). The K-L analysis shows that the ORR proceeds under the diffusion control at $E < -0.1 \,\mathrm{V}$ and in the mixed kineticdiffusion conditions at E > -0.1 V. The K–L equation (see Equation S1) [56] with the values of constants corresponding to 0.1 M KOH [57] was used to calculate the electron transfer number (n) from the slopes of the K–L lines. The n value is gradually approaching 4 at more negative potentials referring to the $2 \times 2e^{-}$ reaction pathway. Furthermore, the chronoamperometric (CA) ORR stability testing at 0.6 V vs. RHE at 960 rpm was performed for Fe/Co-PDC-N and Fe/Mn-PDC-N catalysts (Figure S10) according to the previously published procedure [24]. The CA test showed the superiority of

Fe/Co-PDC-N as the ORR catalyst over Fe/Mn-PDC-N and also over similar Fe/Co-NGr-3 (19% decline in current) from previous investigation [24].

The OER activity of the double TM-containing precursor PDC materials (Figure 5a, Table 3) is quite considerable (Fe/Co-PDC is on par with Pt-Ru/C at 10 mA cm⁻²), which is also consistent with the previous reports on single TM-based PDC catalysts [25, 27]. However, very low activity is observed in the case of TM-free PDC material indicating the importance of TM species (e.g., TM oxides, Figure S3) to provide high OER performance in the PDCs. After the functionalisation with N (Figure 5b, Table 3), the increase in the OER activity is observed, which can be expected as the N species with the coordination to TM (e.g., M-N_x) and without (e.g., pyridinic) have been reported to be responsible for high OER performance [5, 47].

For the combined evaluation of the catalysts ORR and OER activity in one numerical value, the ORR/OER potential gap (ΔE) can be used, which is the difference between the $E_{1/2}$ (determined for ORR at -3 mA cm^{-2}) and $E_{j=10}$ (determined for OER at 10 mA cm⁻²) values [24, 25]. In the present work, the ΔE for the catalysts were optimised towards the lower values by comparing the binary TM catalysts modified with DCDA at two different pyrolysis temperatures (Figure S8). The optimised pyrolysis temperatures were found as 800°C for Fe/Cu-PDC-N and Fe/Mn-PDC-N, while Fe/Co-PDC-N exhibited lower ΔE value when prepared at 900°C. Therefore, these were the carbonisation temperatures used for the preparation of specific catalysts in the present investigation (Figure 5b, Table 3). The lowest ΔE value of 0.87 V is obtained in the case of Fe/Co-PDC-N, which is very similar to the ΔE value of Pt-Ru/C and to the ones in previous studies for PDCbased Ni/SiOC [27] and also to Fe, Co, and N co-doped graphene-coated alumina nanofibers prepared using DCDA $(\Delta E = 0.85 - 0.88 \text{ V})$ [24]. Additional ORR and OER experiments with Fe/Co-PDC-N and Fe/Co-PDC-N catalysts in $1.0\,\mathrm{M}$ KOH were performed (Figure S9). The $E_{1/2}$ value in $1.0 \,\mathrm{M}$ KOH is determined at $-2 \,\mathrm{mA \, cm}^{-2}$ due the ca. 33% lower diffusion-limiting current compared to 0.1 M KOH caused by the lower O_2 solubility [58, 59]. Still, the lower $E_{1/2}$ value of 0.60 V was found for Fe/Co-PDC-N compared to 0.1 M KOH (0.76 V). The superior $E_{j=10}$ value of 1.58 V in 1.0 M KOH was witnessed indicating to the more favourable OER kinetics in highly alkaline conditions. Despite the latter, the moderate ΔE value of 0.98 V was calculated in 1.0 M KOH. Increasing the catalyst loading to 0.4 mg cm⁻² had surprisingly negative effect on the OER/ORR performance indicating that 0.2 mg cm⁻² is the sufficient loading for this type of measurement.

In addition to the evaluation of the ΔE value, the electrochemical double-layer capacitance ($C_{\rm dl}$) can be estimated to assess the suitability of one catalyst over another for the RZAB air electrode application (Figures 7, S11, S12) [60, 61]. The binary TM-containing PDC materials before the N functionalisation exhibit the $C_{\rm dl}$ values of ca. 2.0 mF cm⁻² for Fe/Mn and Fe/Co combinations, while lower $C_{\rm dl}$ value of 1.2 mF cm⁻² is obtained for Fe/Cu material. These values are in good agreement with the 1.5 mF cm⁻² reported in an earlier

study for 5 wt%-Ni/PDC [25]. After the functionalisation with N using DCDA, the $C_{\rm dl}$ values have increased by ~ 70% for all the catalysts with Fe/Mn-PDC-N showing the highest value (3.3 mF cm $^{-2}$), which is followed by Fe/Co-PDC-N (3.0 mF cm $^{-2}$). The increase in the $C_{\rm dl}$ value is most likely due to the new high specific surface area nanocarbon material formation (e.g., CNTs) during the carbonisation with DCDA as evidenced by different physicochemical characterisation techniques (Section 3.1) and indicates that Fe/Co- and Fe/Mn-based materials could host higher amount of electroactive sites for ORR/OER compared to the Fe/Cu-PDC-N catalyst [24, 25].

3.3. RZAB Testing. In this work, the in-house built liquid electrolyte RZAB setup was modified with electrolyte contact to the both sides of Zn-foil and electrolyte compartment ventilation tubes (Section 2.3.2) compared to the previous RZAB cell version used in our earlier investigations [24, 37, 38]. These modifications were firstly evaluated with a commercial Pt-Ru/ C air electrode. The solid black line (Pt-Ru/C) in Figures 8, S13 stands for the data obtained with the modified RZAB unit cell, and the grey dashed line (Pt-Ru/C*) to the original nonmodified version of the cell. Firstly, the open circuit voltage (OCV) value (1.48 V, Table 4) is increased compared to the original cell (1.45 V, Pt-Ru/C* [24, 38]). According to the discharge polarisation curve (Figure 8a), the cut-off point at ca. 200 mA cm⁻² is avoided and additionally higher cell voltage is recorded at lower current densities (inset to Figure 8a) with the modified RZAB configuration. Among the N-doped binary TM-containing PDC materials, the Fe/Co-PDC-N air electrode catalyst exhibits the highest voltage throughout the polarisation curve, which is in accordance with the ORR half-cell study results in 0.1 M KOH (Figure 5b, Table 3). Corresponding tendencies are also carried forward to the calculated power curves (Figure 8b), where the maximum power density $(P_{\rm max})$ values of 154 and 142 mW cm⁻² for Pt-Ru/C and Fe/Co-PDC-N, respectively, are obtained (Table 4).

The total discharge experiment at constant -20 mA cm⁻² (Figure 8c) shows once again the superiority of the modified RZAB cell configuration very likely due to the more favourable consumption of the Zn-foil on both sides and at the edges of 4 mm hole in the foil. The evaluation of the total discharge data was performed according to the method published by Parker et al. [68], taking into consideration the total amount of Zn-foil available for the electrolyte contact (Table 4). The Pt-Ru/C air electrode exhibited the highest mean cell discharge voltage (McdV), while all N-doped double TM-containing PDC materials showed superior specific capacity (SC), specific energy (SE) and depth of discharge (DoD). The optimal material is considered to be Fe/Co-PDC-N due to the high capacities, DoD (97%) and the McdV is the second one from Pt-Ru/C (e.g., 11th hour in the inset to Figure 8c). The high DoD values in the modified cell compared to the original design could be also favoured by the 2 times higher electrolyte volume as Zn-foil passivation is also influenced by the critical zincate concentration and ZnO solubility in the electrolyte according to the recent work by Fuchs et al. [69]. The recharge polarisation curves were recorded at least 15 min after the total discharge experiment at constant -20 mA cm⁻² (Figure 8c) and the

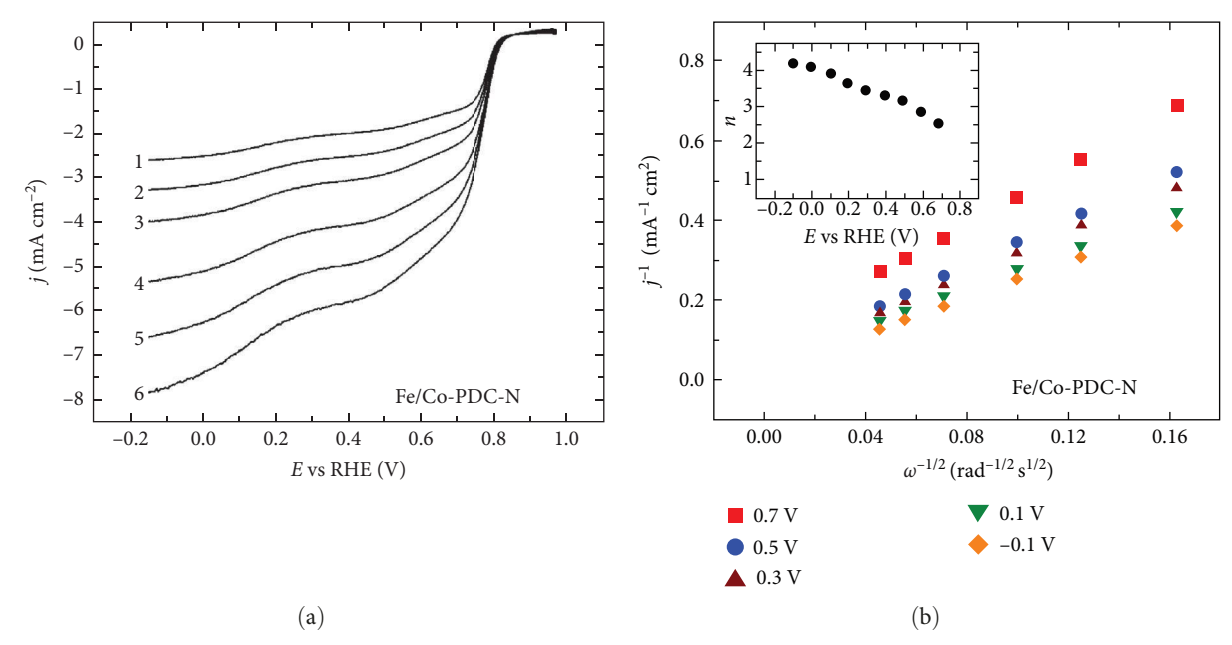


FIGURE 6: (a) RDE polarisation curves ($\nu = 10 \text{ mV s}^{-1}$) at (1) 360, (2) 610, (3) 960, (4) 1900, (5) 3100, (6) 4600 rpm for O₂ reduction on Fe/Co-PDC-N catalyst-coated GC electrodes in O₂-saturated 0.1 M KOH, catalyst loading 0.2 mg cm⁻². (b) Koutecky–Levich plots derived from the corresponding RDE polarisation curves in Figure 6a, the inset shows the potential dependence of the electron transfer number (n).

obtained recharge curves are presented in Figure 8d. According to this experiment, the rechargeability of Fe/Co-PDC-N is more beneficial due to the lower voltage compared to Pt-Ru/C at higher *j* values than 75 mA cm⁻².

The charge-discharge cycling was performed using the current density of 10 mA cm⁻² and total one-cycle duration of 1 h and the superiority of the modified RZAB cell configuration was once more witnessed as the lifespan of Pt-Ru/C air electrode containing cell increased 10 times from 6 h (Fig. S13a) to 57 h (Figure 8e, Table 4). In accordance, similar lifespan of ca. 5.5 h before the 1st mechanical recharge was also measured for Pt-Ru/C using 5 mA cm⁻² and total one cycle length of 10 min in an earlier report with the original RZAB setup [38]. In addition to the higher electrolyte volume and more accessible Zn-foil, the 10 times increase in the lifespan of the cell could also be due to the added ventilation to the electrolyte chambers. More specifically, during charging O₂ evolves from the air electrode and discharging can be accompanied by H₂ evolution at the Zn-foil, which can both cause overpressure or gas bubble formation in the electrolyte compartment [28, 70].

The charge–discharge voltage gap (ξ) and the corresponding energy utilisation efficiency (i.e., round-trip efficiency, ε) are two parameters to describe the RZAB performance changes through the cycling lifespan (Figure S13) [24, 62]. During the second cycle (Figures 8e, S13b), the N-doped double TM-containing PDC air electrodes follow the same activity order towards the OER as observed in 0.1 M KOH (Figure 5b, Table 3), while Pt-Ru/C is superior to all of them. In the case of discharge voltage (ORR), only the superiority of Pt-Ru/C can be distinguished. At the 16th hour (Figures 8e, S13c), the ORR/OER behaviour of PDC materials resembles more closely the one of Pt-Ru/C (similar ξ and ε values) evidencing the superiority in the long-term cycling durability of the N-doped double TM-containing PDCs. The better durability of the PDC

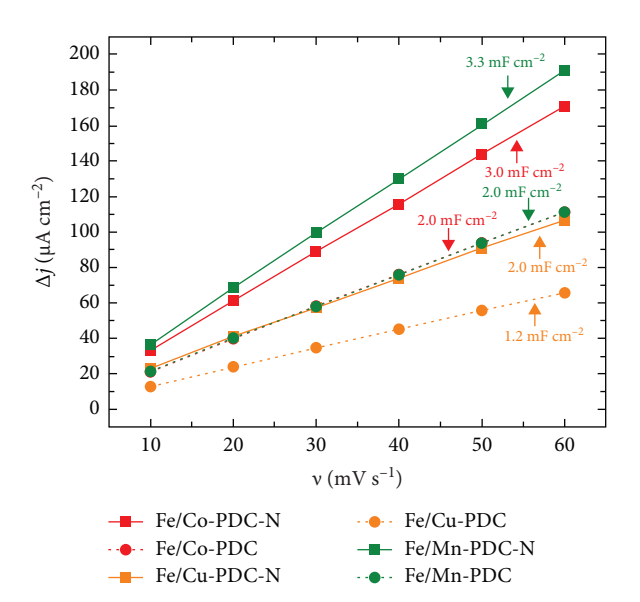


FIGURE 7: $C_{\rm dl}$ values and the dependence of scan rate on the average value of cathodic and anodic current density (Δj) at 0.915 V from the CVs recorded in Ar-saturated 0.1 M KOH solution shown in Figure S11. Unmodified double TM-containing PDC materials (dotted line) and their N-doped derivatives (solid line).

materials could be influenced by the higher oxidation and corrosion resistance of SiOC backbone compared to the compressed carbon black-based Pt-Ru/C with potential carbon corrosion. During the 31st hour (Figures 8e, S13d), the difference between Pt-Ru/C and Fe/Co-PDC-N air electrode performance is almost indistinguishable (similar ξ and ε values), while the Fe/Mn- and Fe/Cu-based catalysts exhibit slightly and considerably lower RZAB performance, respectively. The

ijer, 2025, 1, Downloaded from https://onlinelibrary.wiley.com/doi/10.1155/er/4252866 by Disch Zentrum F. Luft-U. Raum Fahrt In D. Helmholtz Gemein., Wiley Online Library on [27/10/2025], See the Terms and Conditions (https://onlinelibrary.wiley.com/etrms-and-conditions) on Wiley Online Library for rules of use governed by the applicable Tecavity Commons.

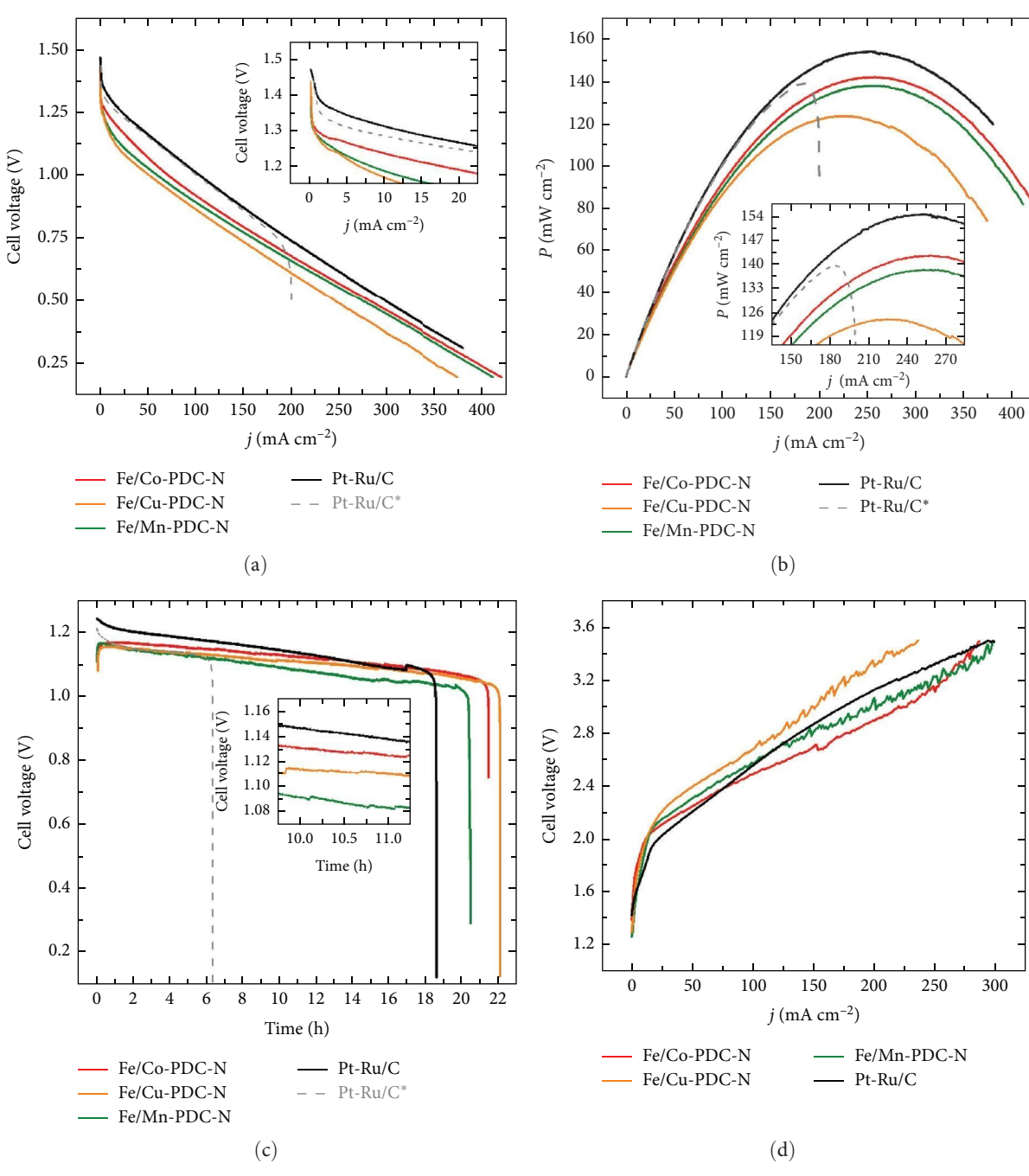


Figure 8: Continued.

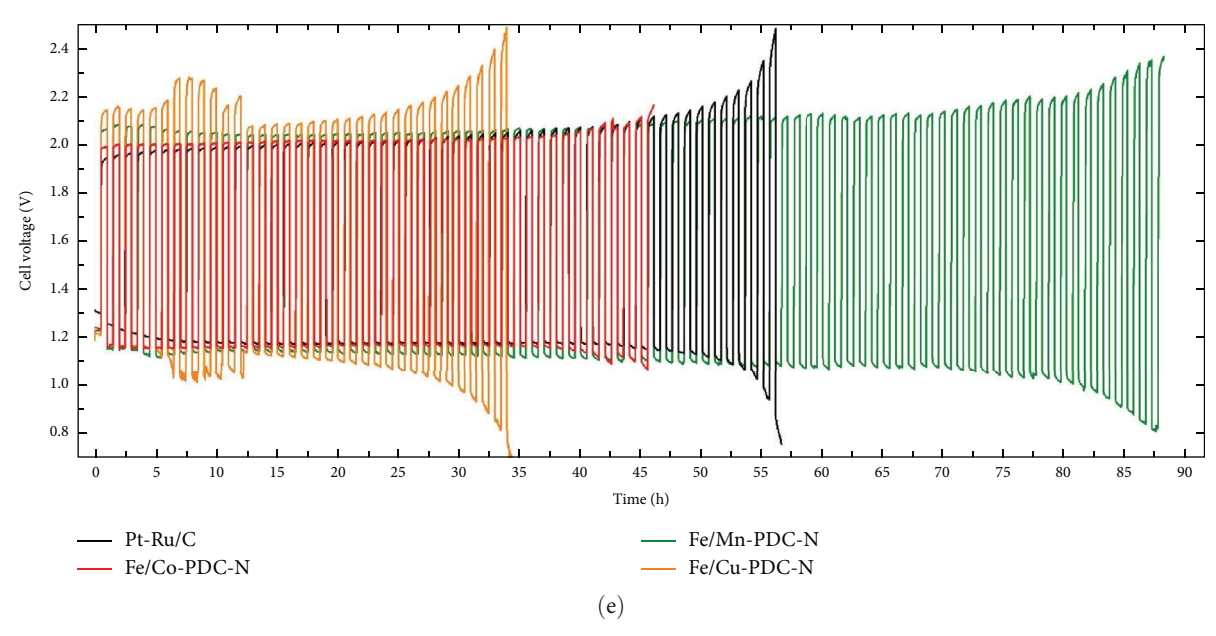


FIGURE 8: Zn–air battery testing with different catalyst material-coated air cathodes: (a) discharge polarisation curves, (b) calculated power density curves, (c) complete discharge at constant $-20 \, \text{mA cm}^{-2}$, (d) recharge polarisation curves after complete discharge, (e) repetitive charge–discharge cycling with $0.5 \, \text{h} - 10 \, \text{and} \, 0.5 \, \text{h} + 10 \, \text{mA cm}^{-2}$. The insets (a–d) show the magnification of the main figures in the specific sections, (*) data for non-modified cell design.

Table 4: Comparison of RZAB characteristics for different (binary) TM-based NPMC air electrodes from this work (Figure 8) and the literature, open circuit voltage (OCV, V) maximum discharge polarisation curve power density (P_{max} , mW cm⁻²), charge–discharge cycling stability cycles or time@j (CycStab, mA cm⁻²), specific capacity (SC, mAh g_{Zn}^{-1}), specific energy (SE, mWh g_{Zn}^{-1}), and depth of discharge (DoD, %).

Catalyst	OCV	$P_{\rm max}$	CycStab	SCb	SEb	DoD^b	Ref.
Pt-Ru/C	1.48	154	57 h@10	691	794	84	This work
Fe/Co-PDC-N	1.55	142	46 h@10	797	895	97	This work
Fe/Cu-PDC-N	1.54	124	34 h@10	821	908	100	This work
Fe/Mn-PDC-N	1.52	138	88 h@10	761	829	93	This work
Ni/PDC	1.24	59	65 h@5 ^a	_	_	_	[25]
H.A.Ni	1.48	110	50 h@2	_	_	_	[26]
Fe/Co-NGr-3	1.39	149	16 h@5 ^a	_	_	_	[24]
FeCoN-PDF-T ₂ -2	1.53	258	25 h@10	_	_		[20]
FePc CNTs NiCo (CP)	1.37	220	700 cycles@10	_	_	_	[62]
FeCo@MNC	1.41	115	24 h@20	_	_	_	[63]
FeCo/N-CNFs	1.45	356	100 h@10	_	_		[64]
FeCoTpp-900-2:IrO ₂	1.41	128	72 h@5	_	_		[65]
Co ₃ Ni ₁ -NC	1.38	123	5000 cycles	_	_	_	[61]
FeCu-NC@XC-72	1.48	191	360 h@1	_	_		[66]
Cu-Fe@CNTs/NC	1.48	167	1000 cycles@2	_	_	_	[60]
$FeCo-N_x$ -CN-30	1.41	150	44 h@10	_	_	_	[67]

^aDetermined until the first electrolyte change or mechanical recharge.

superiority of the Fe/Co-PDC-N catalyst over its PDC derivatives is consistent with the ORR/OER half-cell and CA stability testing results obtained in 0.1 M KOH (Table 3, Figure S10) and could be mainly attributed to the highest N content found by the EDX and XPS methods (Tables 1 and 2) and the superiority of Fe co-doping with Co compared to Mn and Cu. Similarly, the Fe/Co combination showed higher ORR activity compared

to Fe/Mn and Fe/Cu in the case of ZIF-8-modified binary TM-containing PDC materials tested at gas diffusion electrode with concentrated $\rm H_3PO_4$ electrolyte at $160^{\circ}C$ [33] indicating the superiority of Fe/Co over wide pH and temperature ranges.

The PDC-based mono TM-containing catalysts have been previously applied at the RZAB air electrode in several investigations, which are also included in Table 4 for comparison

^bThese values are calculated according to the route from Parker et al. [68].

[25, 26]. The RZAB performance data obtained in the present work is superior to both previous investigations, although it should be noted that the specific conditions for the RZAB testing and setup can have a tremendous impact on the battery characteristics as observed herein for comparative Pt-Ru/C and Pt-Ru/C* experiments (Figures 8, S13a). Therefore, also the RZAB testing results with various types of more active NPMC air electrodes superior to the data presented within the present work can be found (Table 4) [5, 20, 62, 71]. Despite the latter, this investigation is an important step forward for the development of applicable (double) TM and N co-doped PDC-based catalysts for the RZAB air electrode and simultaneously advancing the RZAB cell design and characterisation techniques.

4. Conclusions

In the present report, three binary TM combinations (Fe/Co, Fe/Mn, Fe/Cu) were investigated for the preparation of PDCs subclass SiOC-based bifunctional electrocatalysts for the RZAB air electrode. Modification with DCDA was used to introduce nitrogen moieties into the catalyst materials via pyrolysis at comparative temperatures of 800 and 900°C. The highest bifunctional activity towards the oxygen reactions was observed in the case of Fe/Co-containing material Fe/Co-PDC-N, which showed the ΔE value of 0.87 V in 0.1 M KOH. The $E_{i=10}$ value for Fe/Co-PDC-N in 1.0 M KOH was 1.58 V. The superiority of Fe/Co-PDC-N over its Fe/Mn and Fe/Cu counterparts was attributed to the specific TM and the highest N content according to the EDX and XPS studies providing the highest amount of ORR/OER active N species (e.g., M-N_x, pyridinic, pyrrolic, etc.). Fe/Co-PDC-N performance in the RZAB was also the closest to the one of commercial Pt-Ru/ C compared to two other binary TM-containing NPMCs. Fe/Co-PDC-N air electrode equipped RZAB discharge polarisation curve showed the P_{max} of 142 mW cm⁻², 46 h lifetime for 10 mA cm⁻² charge-discharge cycling, and 97% depth of discharge. Pt-Ru/C air electrode containing RZAB exhibited $P_{\rm max}$ of 142 mW cm⁻², 57 h lifetime for 10 mA cm⁻² charge-discharge cycling, and 84% depth of discharge. Furthermore, in the present investigation, two RZAB design modifications were introduced, which favoured the RZAB performance. The modifications were electrolyte compartment ventilation and electrolyte access to both sides of the Zn foil.

Data Availability Statement

The data that support the findings of this study are available from the corresponding author upon reasonable request.

Conflicts of Interest

The authors declare no conflicts of interest.

Funding

This study was supported by Estonian Research Council, Grants PUTJD1170, PRG2569, PRG2594, PRG1509; German Academic Exchange Service, DLR-DAAD Research Fellowship No. 521; Deutsches Zentrum für Luft- und Raumfahrt, DLR-

DAAD Research Fellowship No. 521; Estonian Ministry of Education and Research, TK210.

Acknowledgments

This study was financially supported by the Estonian Research Council grants (PUTJD1170, PRG2569, PRG2594, and PRG1509). M. M. acknowledges DLR and the German Academic Exchange Service (DAAD) for the funding via DLR-DAAD Research Fellowship No. 521. This research was also supported by the Estonian Ministry of Education and Research (TK210, Centre of Excellence in Sustainable Green Hydrogen and Energy Technologies). We would like to thank the following experts at the University of Tartu, Dr. Heiki Erikson for providing the battery cell for the RZAB investigations, Marian Külaviir and Dr. Peeter Paaver for performing the MP-AES measurements.

Supporting Information

Additional supporting information can be found online in the Supporting Information section. (Supporting Information) Supporting information includes Koutecky–Levich equation (S1), tables and figures for Fe/Co-PDC, Fe/Cu-PDC, Fe/Mn-PDC materials and their DCDA functionalised derivatives (-N). Tables S1 and S2 show electrocatalyst precursor solution composition (wt%) and bulk composition by EDX (wt%) for different PDC catalysts. Figures S1-S3 include deconvoluted Raman spectra, N2 adsorption-desorption isotherms, and XRD patterns for several catalysts, respectively. Figures S4-S7 exhibit SEM and TEM images for PDC and PDC-N samples. Figures S8-S10 include RDE and CA results in 0.1 M and 1.0 M KOH for PDC and PDC-N materials. Figures S11 and S12 include CV results in 0.1 M KOH for PDC and PDC-N materials. Figure S13 shows repetitive charge-discharge cycling data for RZAB with Pt-Ru/C and PDC-N air electrode catalysts.

References

- [1] D. Qiu, H. Wang, T. Ma, et al., "Promoting Electrocatalytic Oxygen Reactions Using Advanced Heterostructures for Rechargeable Zinc-Air Battery Applications," *ACS Nano* 18, no. 33 (2024): 21651–21684.
- [2] J. Axsen, C. Bhardwaj, and C. Crawford, "Comparing Policy Pathways to Achieve 100% Zero-Emissions Vehicle Sales by 2035," Transportation Research Part D: Transport and Environment 112 (2022): 103488.
- [3] M. Alemu, A. Worku, and M. Getie, "Recent Advances in Electrically Rechargeable Transition Metal-Based-Air Batteries for Electric Mobility," *Inorganic Chemical Communications* 159 (2024): 111742.
- [4] G. Nazir, A. Rehman, J. Lee, et al., "A Review of Rechargeable Zinc-Air Batteries: Recent Progress and Future Perspectives," *Nano-micro letters* 16, no. 1 (2024): 138.
- [5] Y. Kumar, M. Mooste, and K. Tammeveski, "Recent Progress of Transition Metal-Based Bifunctional Electrocatalysts for Rechargeable Zinc-Air Battery Application," *Current Opinion* in Electrochemistry 38 (2023): 101229.
- [6] E. Davari and D. Ivey, "Bifunctional Electrocatalysts for Zn-Air Batteries," Sustainable Energy Fuels 2, no. 1 (2018): 39–67.

2025, 1, Downloaded from https://onlinelibrary.wiley.com/doi/10.1155/er/422866 by Disch Zantrum F. Luft-U. Raum Fahrt In D. Helmholtz Gemein., Wiley Online Library on [27/10/2025]. See the Terms and Conditions (https://onlinelibrary.wiley.com/terms-and-conditions) on Wiley Online Library for rules of use; OA article are governed by the applicable Pearative Commons.

- [7] S. Zago, L. C. Scarpetta-Pizo, J. H. Zagal, and S. Specchia, "PGM-Free Biomass-Derived Electrocatalysts for Oxygen Reduction in Energy Conversion Devices: Promising Materials," *Electrochemical Energy Reviews* 7, no. 1 (2024): 1.
- [8] S. Haller, V. Gridin, K. Hofmann, R. W. Stark, B. Albert, and U. I. Kramm, "Application of Non-Precious Bifunctional Catalysts for Metal-Air Batteries," *Energy Technology* 9, no. 7 (2021): 2001106.
- [9] Q. Liu, L. Wang, and H. Fu, "Research Progress on the Construction of Synergistic Electrocatalytic ORR/OER Self-Supporting Cathodes for Zinc-Air Batteries," *Journal of Materials Chemistry A* 11, no. 9 (2023): 4400–4427.
- [10] B. Saravanakumar, K. Thiyagarajan, S. Balasingam, T. Siva, R. Pai, and A. Ramadoss, "Recent Advances and Innovations in the Piezoelectrochemical Process for Energy and the Environment: A Review," *Journal of Energy Storage* 83 (2024): 110576.
- [11] K. Kisand, A. Sarapuu, J. Douglin, et al., "Hierarchically Porous Fe—N—C Single-Atom Catalysts via Ionothermal Synthesis for Oxygen Reduction Reaction," *ChemSusChem* 18, no. 2 (2025): e202401332.
- [12] S. S.Dongre, G. Zuccante, M. Muhyuddin, et al., "Innovative Biochar-Based Electrocatalysts From Chilli Plants and Fruits for Sustainable Oxygen Reduction and Hydrogen Evolution Reactions," *Electrochimica Acta* 517 (2025): 145763.
- [13] D. Wang, X. Pan, P. Yang, et al., "Transition Metal and Nitrogen Co-Doped Carbon-Based Electrocatalysts for the Oxygen Reduction Reaction: From Active Site Insights to the Rational Design of Precursors and Structures," *ChemSusChem* 14, no. 1 (2021): 33–55.
- [14] S. D. Bhoyate, J. Kim, F. M. de Souza, et al., "Science and Engineering for Non-Noble-Metal-Based Electrocatalysts to Boost Their ORR Performance: A Critical Review," Coordination Chemistry Reviews 474 (2023): 214854.
- [15] M. Alam, K. Ping, M. Danilson, et al., "Iron Triad-Based Bimetallic M–N–C Nanomaterials as Highly Active Bifunctional Oxygen Electrocatalysts," ACS Applied Energy Materials 7, no. 9 (2024): 4076–4087.
- [16] S. Asaithambi, P. Sakthivel, M. Karuppaiah, et al., "Investigation of Electrochemical Properties of Various Transition Metals Doped SnO₂ Spherical Nanostructures for Supercapacitor Applications," *Journal of Energy Storage* 31 (2020): 101530.
- [17] S. Asaithambi, P. Sakthivel, M. Karuppaiah, et al., "Preparation of Fe-SnO2@CeO2 Nanocomposite Electrode for Asymmetric Supercapacitor Device Performance Analysis," *Journal of Energy Storage* 36 (2021): 102402.
- [18] R. Kumar, M. Mooste, Z. Ahmed, et al., "Highly Active ZIF-8@CNT Composite Catalysts as Cathode Materials for Anion Exchange Membrane Fuel Cells," *Industrial Chemistry & Materials* 1 (2023): 526–541.
- [19] Y. Kumar, E. Kibena-Põldsepp, M. Mooste, et al., "Iron and Nickel Phthalocyanine-Modified Nanocarbon Materials as Cathode Catalysts for Anion-Exchange Membrane Fuel Cells and Zinc-Air Batteries," *ChemElectroChem* 9, no. 20 (2022): e202200717.
- [20] Y. Kumar, S. Akula, J. Kozlova, et al., "Zinc-Assisted Synthesis of Polymer Framework-Based Atomically Dispersed Bimetal Catalysts for Efficient Oxygen Electrocatalysis in Rechargeable Zinc-Air Batteries," *Journal of Energy Storage* 86 (2024): 111164.
- [21] Z. Ahmed, J. Kozlova, K. Kukli, et al., "Boosting Bifunctional Oxygen Electrocatalysis by Integrating Fe-Nx Moieties and

- FeNi Nanoparticles for Highly Efficient and Long-Life Rechargeable Zinc-Air Batteries," *Sustainable Energy & Fuels* 9, no. 8 (2025): 2098–2108.
- [22] W. Y. Zhang, Y. G. Chao, W. S. Zhang, et al., "Emerging Dual-Atomic-Site Catalysts for Efficient Energy Catalysis," *Advanced Materials* 33, no. 36 (2021): 2102576.
- [23] T. Canuto de Almeida e Silva, M. Mooste, E. Kibena-Põldsepp, et al., "Polymer-Derived Co/Ni–SiOC(N) Ceramic Electrocatalysts for Oxygen Reduction Reaction in Fuel Cells," *Catalysis Science & Technology* 9, no. 3 (2019): 854–866.
- [24] M. Mooste, Z. Ahmed, P. Kapitulskis, et al., "Bifunctional Oxygen Electrocatalyst Based on Fe, Co, and Nitrogen Co-Doped Graphene-Coated Alumina Nanofibers for Zn-Air Battery Air Electrode," Applied Surface Science 660 (2024): 160024.
- [25] P. Moni, M. Mooste, K. Tammeveski, K. Rezwan, and M. Wilhelm, "One-Dimensional Polymer-Derived Ceramic Nanowires With Electrocatalytically Active Metallic Silicide Tips as Cathode Catalysts for Zn-Air Batteries," RSC Advances 11, no. 63 (2021): 39707–39717.
- [26] P. Moni, M. G. Pollachini, M. Wilhelm, et al., "Metal-Containing Ceramic Composite With in Situ Grown Carbon Nanotube as a Cathode Catalyst for Anion Exchange Membrane Fuel Cell and Rechargeable Zinc-Air Battery," ACS Applied Energy Materials 2, no. 8 (2019): 6078–6086.
- [27] S. Abinaya, P. Moni, V. Parthiban, A. K. Sahu, and M. Wilhelm, "Metal Silicide Nanosphere Decorated Carbon-Rich Polymer-Derived Ceramics: Bifunctional Electrocatalysts Towards Oxygen and Their Application in Anion Exchange Membrane Fuel Cells," *ChemElectroChem* 6, no. 13 (2019): 3268–3278.
- [28] M. Deyab and Q. Mohsen, "Reducing Corrosion and Hydrogen Gas Release Inside an Alkaline Zinc-Air Battery by Employing Ionic Liquid," *Electrochimica Acta* 508 (2024): 145207.
- [29] Y. Jo, K. Prasanna, S. Kang, et al., "The Effects of Mechanical Alloying on the Self-Discharge and Corrosion Behavior in Zn-Air Batteries," *Journal of Industrial and Engineering Chemistry* 53 (2017): 247–252.
- [30] M. Bockelmann, L. Reining, U. Kunz, and T. Turek, "Electrochemical Characterization and Mathematical Modeling of Zinc Passivation in Alkaline Solutions: A Review," *Electrochimica Acta* 237 (2017): 276–298.
- [31] H. Yang, Y. Cao, X. Ai, and L. Xiao, "Improved Discharge Capacity and Suppressed Surface Passivation of Zinc Anode in Dilute Alkaline Solution Using Surfactant Additives," *Journal* of Power Sources 128, no. 1 (2004): 97–101.
- [32] S. Huang, P. Pei, and Z. Wang, "Anode Corrosion of Zn-Air Fuel Cell: Mechanism and Protection," *Journal of the Electrochemical Society* 167, no. 9 (2020): 090538.
- [33] M. Mooste, J. Müller-Hülstede, D. Schonvogel, et al., "Binary Transition Metal and ZIF-8 Functionalised Polymer-Derived Ceramic Catalysts for High Temperature PEM Fuel Cell Cathode," *Electrochimica Acta* 514 (2025): 145620.
- [34] A. Sadezky, H. Muckenhuber, H. Grothe, R. Niessner, and U. Pöschl, "Raman Micro Spectroscopy of Soot and Related Carbonaceous Materials: Spectral Analysis and Structural Information," *Carbon* 43, no. 8 (2005): 1731–1742.
- [35] M. Mooste, E. Kibena-Põldsepp, V. Vassiljeva, et al., "Electrocatalysts for Oxygen Reduction Reaction Based on Electrospun Polyacrylonitrile, Styrene–Acrylonitrile Copolymer and Carbon Nanotube Composite Fibres," *Journal of Materials Science* 54, no. 17 (2019): 11618–11634.

- [36] N. Shrestha, S. Patil, J. Han, et al., "Chemical Etching Induced Microporous Nickel Backbones Decorated With Metallic Fe@hydroxide Nanocatalysts: An Efficient and Sustainable OER Anode Toward Industrial Alkaline Water-Splitting," Journal of Materials Chemistry A 10, no. 16 (2022): 8989–9000.
- [37] J.-M. Assafrei, G. Yusibova, K. Ping, et al., "Maximizing the Performance of Aqueous Zinc-Air/Iodide Hybrid Batteries Through Electrolyte Composition Optimization," *Journal of Energy Storage* 74 (2023): 109528.
- [38] K. Muuli, R. Kumar, M. Mooste, et al., "Iron, Cobalt, and Nickel Phthalocyanine Tri-Doped Electrospun Carbon Nanofibre-Based Catalyst for Rechargeable Zinc–Air Battery Air Electrode," *Materials* 16, no. 13 (2023): 4626.
- [39] S. Y. Zhao, Y. Cheng, J. P. Veder, et al., "One-Pot Pyrolysis Method to Fabricate Carbon Nanotube Supported Ni Single-Atom Catalysts With Ultrahigh Loading," ACS Applied Energy Materials 1, no. 10 (2018): 5286–5297.
- [40] H. Nguyen, J. Lee, E. Kwon, et al., "Bamboo-Like N-Doped Carbon Nanotube-Confined Cobalt as an Efficient and Robust Catalyst for Activating Monopersulfate to Degrade Bisphenol A," Chemosphere 279 (2021): 130569.
- [41] S. Li, C. Feng, Y. Xie, C. Guo, A. Hassan, and J. Wang, "Dicyandiamide-Assisted Synthesis of N-Doped Porous CoMn-Nx@N-C Carbon Nanotube Composites via MOFs as Efficient Trifunctional Electrocatalysts in the Same Electrolyte," *Nanoscale* 15, no. 3 (2023): 1210–1220.
- [42] T. Moriai, T. Tsukamoto, K. Fukuhara, T. Imaoka, T. Kambe, and K. Yamamoto, "Carbon Nanotube Growth Catalyzed by Metal Nanoparticles Formed via the Seed Effect of Metal Clusters," *Nanoscale Advances* 7, no. 1 (2024): 346–353.
- [43] Y. Meng, J. X. An, P. X. Hou, C. Liu, and J. C. Li, "Atomically Dispersed Fe/Co—N—C and Their Composites for Proton Exchange Membrane Fuel Cells," *Materials Chemistry Frontiers* 8, no. 8 (2024): 1927–1949.
- [44] L. L. Chen, Y. L. Zhang, L. L. Dong, et al., "Synergistic Effect Between Atomically Dispersed Fe and Co Metal Sites for Enhanced Oxygen Reduction Reaction," *Journal of Materials Chemistry A* 8, no. 8 (2020): 4369–4375.
- [45] R. Kumar, M. Mooste, I. Zekker, et al., "Tailoring Highly Efficient ZIF-Derived FexCey@N-C Composite Catalysts for Oxygen Reduction Reaction in H-Shape Microbial Fuel Cells," International Journal of Hydrogen Energy 98 (2025): 793–806.
- [46] S. Akula, M. Mooste, J. Kozlova, et al., "Transition Metal (Fe, Co, Mn, Cu) Containing Nitrogen-Doped Porous Carbon as Efficient Oxygen Reduction Electrocatalysts for Anion Exchange Membrane Fuel Cells," Chemical Engineering Journal 458 (2023): 141468.
- [47] X. S. Guo, Z. Y. Huang, X. W. Qi, L. P. Si, H. Zhang, and H. Y. Liu, "The Optimization of Iron porphyrin@MOF-5 Derived Fe-N-C Electrocatalysts for Oxygen Reduction Reaction in Zinc-Air Batteries," *Journal of Electroanalytical Chemistry* 936 (2023): 117381.
- [48] J. Wang, Z. Q. Huang, W. Liu, et al., "Design of N-Coordinated Dual-Metal Sites: A Stable and Active Pt-Free Catalyst for Acidic Oxygen Reduction Reaction," *Journal of the American Chemical Society* 139, no. 48 (2017): 17281–17284.
- [49] L. C. P. Pérez, N. R. Sahraie, J. Melke, et al., "Polyformamidine-Derived Non-Noble Metal Electrocatalysts for Efficient Oxygen Reduction Reaction," *Advanced Functional Materials* 28, no. 22 (2018): 1707551.
- [50] Z. Jiang, X. R. Liu, X. Z. Liu, et al., "Interfacial Assembly of Binary Atomic Metal-Nx Sites for High-Performance Energy Devices," *Nature Communications* 14, no. 1 (2023).

- [51] J. G. Buschermöhle, J. Müller-Hülstede, H. Schmies, et al., "Fe–Sn–N–C Catalysts: Advancing Oxygen Reduction Reaction Performance," ACS Catalysis 15 (2025): 4477–4488.
- [52] S. Kabir, K. Artyushkova, A. Serov, and P. Atanassov, "Role of Nitrogen Moieties in N-Doped 3D-Graphene Nanosheets for Oxygen Electroreduction in Acidic and Alkaline Media," ACS Applied Materials & Interfaces 10, no. 14 (2018): 11623– 11632.
- [53] J. H. Zagal and M. T. M. Koper, "Reactivity Descriptors for the Activity of Molecular MN4 Catalysts for the Oxygen Reduction Reaction," *Angewandte Chemie International Edition* 55, no. 47 (2016): 14510–14521.
- [54] C. Z. Loyola, S. Ureta-Zanartu, J. H. Zagal, and F. Tasca, "Activity Volcano Plots for the Oxygen Reduction Reaction Using FeN4 Complexes: From Reported Experimental Data to the Electrochemical Meaning," *Current Opinion in Electrochemistry* 32 (2022): 100923.
- [55] T. F. Li, Y. J. Lv, J. H. Su, et al., "Anchoring CoFe₂O₄ Nanoparticles on N-Doped Carbon Nanofibers for High-Performance Oxygen Evolution Reaction," *Advanced Science* 4, no. 11 (2017): 1700226.
- [56] K. Szwabińska and G. Lota, "Mixed Diffusion-Kinetic Control of H₂O₂ Oxidation at an Oxide-Covered Platinum Electrode in Alkaline Electrolyte: Implications for Oxygen Electroreduction Studies With a Rotating Ring Disk Electrode," *ChemElectroChem* 8, no. 5 (2021): 839–849.
- [57] Y. Kumar, S. Akula, E. Kibena-Põldsepp, et al., "Cobalt Phthalocyanine-Doped Polymer-Based Electrocatalyst for Rechargeable Zinc-Air Batteries," *Materials* 16, no. 14 (2023): 5105.
- [58] C. Alegre, A. Stassi, E. Modica, C. Lo Vecchio, A. Aricò, and V. Baglio, "Investigation of the Activity and Stability of Pd-Based Catalysts Towards the Oxygen Reduction (ORR) and Evolution Reactions (OER) in Iron-Air Batteries," RSC Advances 5, no. 32 (2015): 25424–25427.
- [59] Q. Wang, H. Guesmi, S. Tingry, D. Cornu, Y. Holade, and S. D. Minteer, "Unveiling the Pitfalls of Comparing Oxygen Reduction Reaction Kinetic Data for Pd-Based Electrocatalysts Without the Experimental Conditions of the Current-Potential Curves," ACS Energy Letters 7, no. 3 (2022): 952–957.
- [60] H. Huang, C. Zhang, Z. Chen, et al., "Boosting Oxygen Reduction Performance by Copper-Iron Co-Doped on ZIF-Derived N-Doped Carbon Nanotubes," *International Journal* of Hydrogen Energy 87 (2024): 588–594.
- [61] Q. Sun, Z. Yang, X. Liu, et al., "Ultrasonic-Assisted Strategy to Enhance Electrocatalytic Performance of CoNi N-Doped Carbon Catalyst in Alkaline Oxygen Reduction Reaction and Zinc-Air Batteries," Surfaces and Interfaces 56 (2025): 105443.
- [62] S. C. Ding, L. He, L. Z. Fang, et al., "Carbon-Nanotube-Bridging Strategy for Integrating Single Fe Atoms and NiCo Nanoparticles in a Bifunctional Oxygen Electrocatalyst Toward High-Efficiency and Long-Life Rechargeable Zinc-Air Batteries," Advanced Energy Materials 12, no. 48 (2022): 2202984.
- [63] C. Li, M. Wu, and R. Liu, "High-Performance Bifunctional Oxygen Electrocatalysts for Zinc-Air Batteries Over Mesoporous Fe/Co-N-C Nanofibers With Embedding FeCo Alloy Nanoparticles," Applied Catalysis B: Environmental 244 (2019): 150–158.
- [64] J. J. Zhang, Y. J. Zhang, C. X. Xu, et al., "Metal-Organic-Framework-Derived Bimetallic Carbon-Based Catalysts as Efficient Oxygen Reduction Reaction Electrocatalysts," *Journal of Alloys and Compounds* 948 (2023): 169721.

2025, 1, Downloaded from https://onlinelibrary.wiley.com/doi/10.1155/er/4/252866 by Dusch Zentrum F. Luft-U, Raum Fahrt In D. Helmboltz Gemein., Wiley Online Library on [27/10/2025]. See the Terms and Conditions (https://onlinelibrary.wiley.com/derms-and for rules of use; OA articles are governed by the applicable Creative Commons

- [65] R. Deb, J. Barman, and G. K. Dutta, "Iron, Cobalt Embedded Nitrogen-Doped Carbon Derived From Conjugated Macrocyclic Polymers as Electrocatalysts for Oxygen Reduction Reaction," *Electrochimica Acta* 508 (2024): 145256.
- [66] Y. Yuan, M. Pan, M. Zhang, et al., "Cu Bimetallic Precursor-Driven Quaternary Active Sites Boost Oxygen Reduction/ Evolution Reaction Bifunctional Catalysts," *Journal of Power Sources* 623 (2024): 235423.
- [67] S. Li, C. Cheng, X. J. Zhao, J. Schmidt, and A. Thomas, "Active Salt/Silica-Templated 2D Mesoporous FeCo-Nx-Carbon as Bifunctional Oxygen Electrodes for Zinc-Air Batteries," Angewandte Chemie International Edition 57, no. 7 (2018): 1856–1862.
- [68] J. F. Parker, J. S. Ko, D. R. Rolison, and J. W. Long, "Translating Materials-Level Performance Into Device-Relevant Metrics for Zinc-Based Batteries," *Joule* 2, no. 12 (2018): 2519–2527.
- [69] D. Fuchs, C. Müller, M. Schaffeld, F. Mahlendorf, and H. Hoster, "New Insights Into Zinc Passivation Through Operando Measured Zincate Concentrations," *Batteries & Supercaps* 7, no. 12 (2024): e202400298.
- [70] Y. Zhong, B. Liu, Z. Zhao, Y. Shen, X. Liu, and C. Zhong, "Influencing Factors of Performance Degradation of Zinc-Air Batteries Exposed to Air," *Energies* 14, no. 9 (2021): 2607.
- [71] X. Zhong, Y. Shao, B. Chen, et al., "Rechargeable Zinc-Air Batteries With an Ultralarge Discharge Capacity per Cycle and an Ultralong Cycle Life," *Advanced Materials* 35, no. 30 (2023): 2301952.